JOURNAL OF AIRCRAFT
Vol. 37, No. 5, September–October 2000

Effect of Sweep on Buffet over Novel Wing Planforms

Michael I. Woods*
University of Bath, Bath, England BA2 7AY, United Kingdom
and
Norman J. Wood†
University of Manchester, Manchester, England M13 9PL, United Kingdom

The results of wind tunnel tests carried out on two semispan models, with sweep angles of 40 and 60 deg, are presented. The planforms of the models have features consistent with likely configurations of future low-observable aircraft. An examination of pressure fluctuations over such aircraft is of particular importance because of the difficulties involved in altering such aircraft late in their design to address problems of excessive buffeting. The dynamic calibration of surface pressure tappings has allowed both mean and unsteady pressures to be measured. Unsteady pressure readings have been analyzed to derive both root-mean-square pressures and spectral information. Peaks in the spanwise root-mean-square pressure distribution are found inboard of the leading edge vortex for each wing. Two additional peaks are present over the more highly swept wing. One of these peaks is coincident with the secondary separation; another is found outboard of the leading edge vortex.

Nomenclature

c_0	=	wing root chord
$\bar{c}$	=	aerodynamic mean chord
f	=	frequency
n_m	=	modified frequency parameter
$\bar{p}$	=	root-mean-square pressure
$p(f)$	=	calibration output (frequency domain)
$p(t)$	=	calibration output (time domain)
q	=	freestream dynamic pressure
$r(f)$	=	frequency response function of tubing
S	=	wing area
s	=	wing semispan
U	=	freestream velocity
x	=	chordwise distance from apex
x_t	=	chordwise location of wingtip
y	=	spanwise distance from Centerline
α	=	incidence

Introduction

IN a short-range combat encounter, aircraft tend to engage in a sequence of head-on passes.[1] After each pass, during which weapons are released, both aircraft attempt to reverse course as quickly as possible to obtain another firing opportunity. Previous-generation rear aspect missiles resulted in a *sustained* turn rate's being of critical importance, with pilots maneuvering to get behind their opponents and thus facilitate weapons release. An example of an aircraft designed during this era is the F-16, which emerged from the U.S. Air Force's Lightweight Fighter program in the early 1970s. However with modern all aspect weaponry, combat effectiveness is more sensitive to attainable *unsteady* performance. Maximum instantaneous turn rates are limited by structural limits at moderate and high Mach numbers and by the maximum attainable lift at low speed. The ability to aim the fuselage independently of flight path allows aircraft to utilize gunfire as an effective weapon, with rapid pitching maneuvers' bringing the weapon to bear as the combating aircraft pass.

In addition to the agility required to improve survivability in short-range combat, the advent of stealth technology has resulted in further constraints on the design of combat aircraft. Aerodynamic performance must be optimized while ensuring that the resulting aircraft has both a small radar cross section (RCS) and a low infrared signature. These low-observable requirements have led to designs such as the B-2 and F-117, which have features like equal leading and trailing edge sweeps and discontinuities along the trailing edges. However, these aircraft are not optimized for the air-superiority role and, although stealthy, their agility is insufficient for a next-generation fighter aircraft.

If aircraft with the planforms required for a low RCS were maneuvered at incidences appropriate for successful short-range combat, it is possible that large amounts of flow-induced excitation (buffet) would be encountered. Should the frequency distribution of the buffet coincide with one or more structural modes, then a significant response of the structure (buffeting) may result. This is clearly undesirable and may result in a reduction of the flight envelope and/or in-service repair or replacement modifications. Such problems have been encountered in the past, particularly with reference to the fins of combat aircraft.[2] Typical fixes involve the utilization of strakes to alter the vortex track or increases in structural strength to separate the fin bending mode and excitation frequency. Both of these approaches are unsatisfactory if a similar problem is encountered on a low-observable aircraft toward the end of the design process. The addition of strakes to a stealthy aircraft has a prohibitive RCS penalty, and the complexity of the internal structure required for a minimum RCS makes increases in structural strength costly from a weight, and hence performance, perspective. It is therefore desirable to predict buffet loads during the early design stages of an aircraft such that they can be accounted for from both strength and fatigue viewpoints during the detailed design process.

Measurements of pressure and velocity fluctuations in vortex-dominated flows have indicated that such flows exhibit distinct characteristic frequencies of excitation,[3,4] particularly when vortex burst is present within the flow. A modified reduced-frequency parameter has been proposed,[2] which has the form

$$n_m = f\bar{c}\sin\alpha/U$$

This parameter, which is sensitive to sweep angle, has origins in investigations of the phenomenon of fin buffeting and represents the center frequency of the buffet at the trailing edge of the delta wing. More recent work investigating wing buffet[5,6] has indicated that the center frequency is inversely proportional to the chordwise location on the wing.

Received 20 July 1999; revision received 15 November 1999; accepted for publication 22 March 2000.

*Lecturer, Department of Mechanical Engineering. Member AIAA.
†Professor, School of Engineering, Oxford Road. Senior Member AIAA.

Experimental Details

A series of wind-tunnel models were fabricated for testing in the University of Bath low-speed wind tunnel. Novel manufacturing techniques were used to expedite model production. The successful development of the dynamic calibration of steady surface pressure measurement systems enabled extensive coverage of the unsteady flowfield over the wings' upper surfaces, with 165 tappings embedded into each model. This was coupled with more conventional techniques for buffeting measurement, flow visualization, and balance measurements to provide a comprehensive suite of experimental data.

Model Construction

The dimensioned planforms of the models are shown in Fig. 1, with the leading and trailing edge sweep angles of each model being 40 and 60 deg for the λ wing and y wing respectively. The models each had a maximum thickness of 50 mm, and they each had constant radius lower surfaces and flat upper surfaces. Leading and trailing edges were sharp. The models were semispan mounted, and a circular splitter plate at a distance of 0.20 m from the wind-tunnel wall served as a symmetry plane.

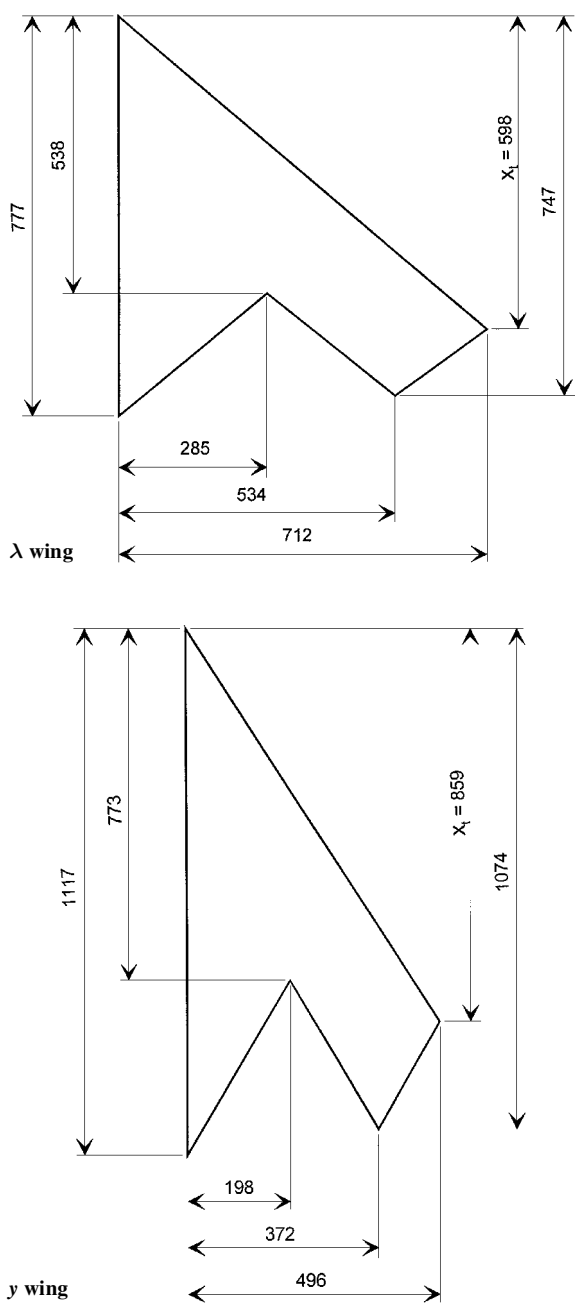

Fig. 1 Planforms dimensions.

Each wing was constructed from a foam core and outer composite skins. A combination of glass and carbon fiber was used, with cold-cured epoxy resins utilized to simplify the manufacturing facilities required. Dimensional accuracy was maintained by the use of templates. This technique enabled lightweight models of high stiffness to be produced quickly and with minimal machining requirements.

For manufacture to be simplified, the upper surface of each model was flat, and tappings were formed on this surface by laying VINL-063 Scanivalve tubes into the Styrofoam IB core of the wing, bonding a glass fiber skin to the surface, and drilling a perpendicular hole directly into the vinyl tube. A carbon fiber skin was bonded to the convex lower surface of each model. In addition to the surface pressure tappings, each model was equipped with six Entran EPE-701-2P pressure transducers, which were co-located with surface pressure tappings, and up to six Entran EGA-125F-25D miniature accelerometers to monitor the buffeting response. Each model took typically two man months to fabricate from start to tunnel entry.

Instrumentation and Data Analysis

Signals from the accelerometers, unsteady pressure transducers, transducers contained within the Scanivalve system, and six-component balance were monitored and controlled by a personal computer-based acquisition system utilizing the software DT-Vee by Data Translation. The system used is shown schematically in Fig. 2. The analog-to-digital(A/D) and digital-to-analog(D/A) subsystem was a DT2839 data-acquisition board by Data Translation. This board was connected to the sensors by means of standard in-house fixed-gain dc amplifier cards and a DT739 terminal panel, also supplied by Data Translation. Surface flow visualization was undertaken by using a suspension on TiO_2 powder in paraffin.

The system for converting unsteady pressure data to power spectral densities (PSDs) is shown schematically in Fig. 3. Static pressure calibrations were applied and fast Fourier transforms (FFTs) calculated within the DT-Vee by software and sent to Microsoft Excel by a dynamic data exchange (DDE) link. Unsteady pressure calibrations were then applied and PSDs calculated within Microsoft Excel. The PSDs were nondimensionalized with the square of the freestream dynamic pressure, allowing the root-mean-square (rms) buffet to be obtained.

Surface Tapping Dynamic Calibration

For unsteady pressures to be measured at a large number of points over the wing, a method previously used at the University of Bath to measure unsteady pressures caused by wing and control surface oscillations[7,8] had to be refined such that significantly higher frequencies could be discerned. Comparisons with surface-mounted unsteady pressure transducers were also required to validate the technique.

The method developed utilized a Scanivalve system, generally used for measuring steady pressure data, to acquire unsteady data. This was achieved by calibrating the vinyl tubing linking the tapping to the pressure transducer. Allowing unsteady pressure contours to be plotted over the surface of the wing required the response function, $r(f)$, of the tubing system connecting the tapping to the pressure transducer within the Scanivalve unit. This would then allow the pressure fluctuations at the tappings to be calculated from the pressure signal measured at the Scanivalve unit.

A new calibration system was derived and is shown schematically in Fig. 4. A signal composed of superposed sine waves with frequencies of 2–500 Hz at 2-Hz increments, each with the same amplitude and random phase, was constructed. This wave was then converted to an analog signal and amplified to drive the speaker. The pressure fluctuations resulting from this input were measured and the spectral content of the oscillations was calculated. The speaker input and the spectra of the pressure fluctuations output from the speaker are

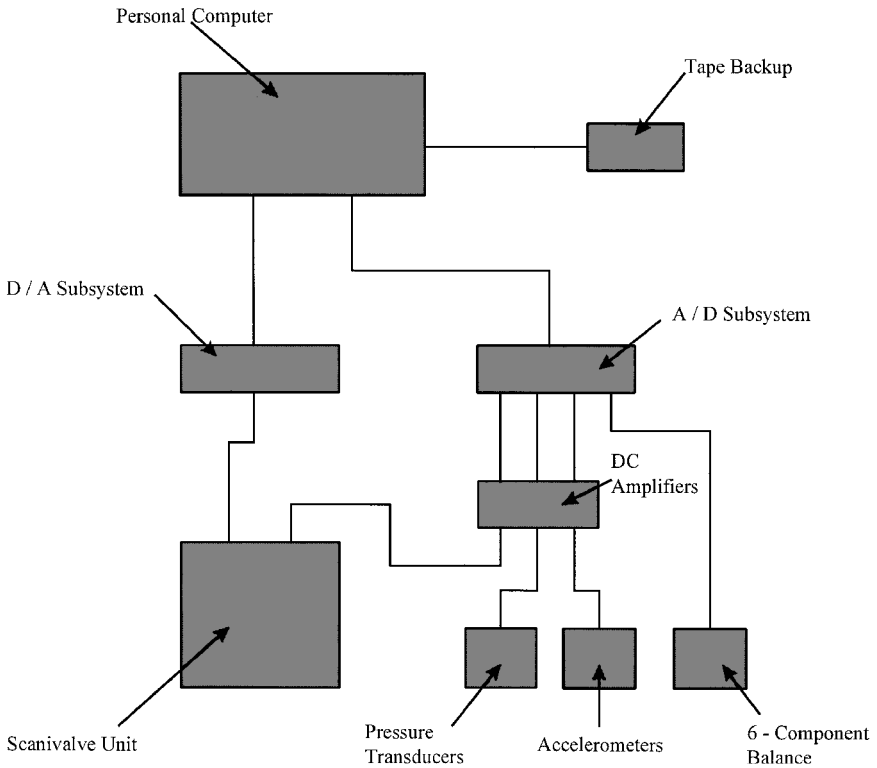

Fig. 2 Data-acquisition system.

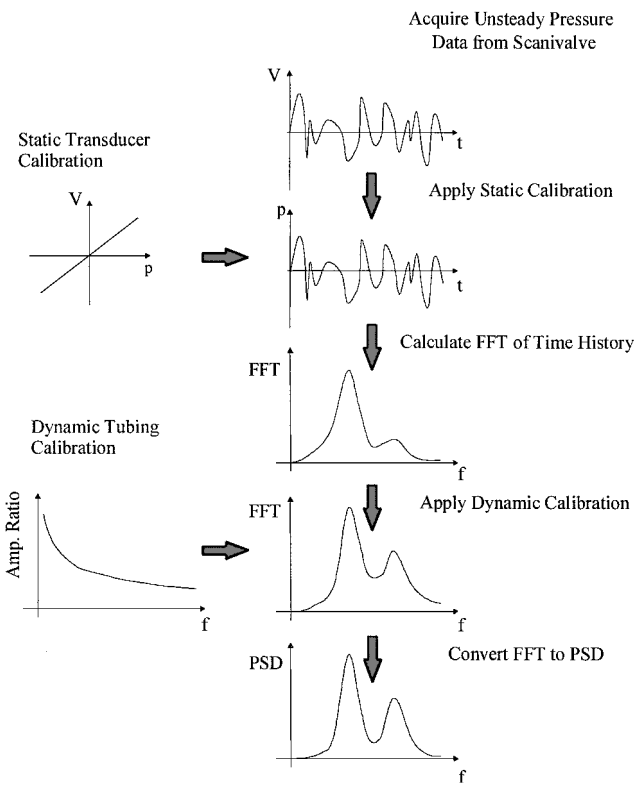

Fig. 3 Unsteady data reduction.

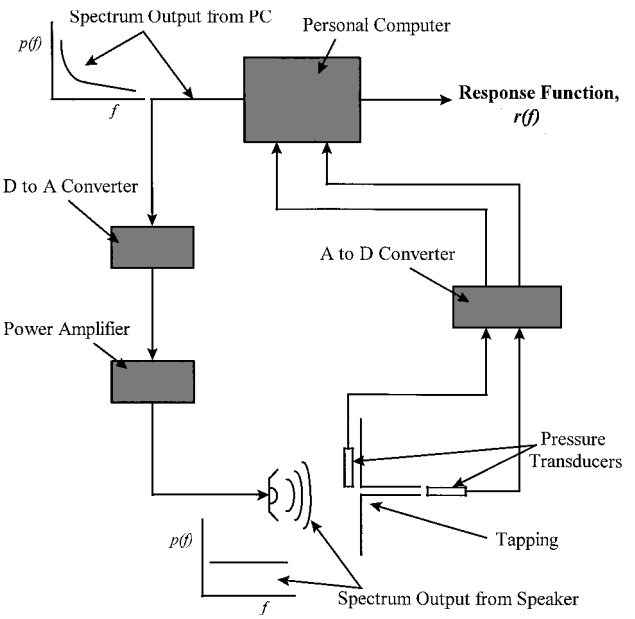

Fig. 4 Tubing calibration system.

depicted in Fig. 5. The white-noise input resulted in pressure fluctuations with little content at low frequencies below approximately 80 Hz and a large spectral content at frequencies above 300 Hz. The response of the speaker could be deduced from these measurements. A new signal was then calculated and generated by the personal computer, tailored to make the amplitude of the pressure oscillation output by the speaker, $p(f)$, constant in the frequency range considered. As is clear from Fig. 5, the speaker was driven extremely hard at low frequencies, with voltage inputs to the speaker approximately four times those in the initial white-noise input at very low frequencies. Similarly, much smaller signals were input in the high-frequency range. This approach resulted in pressure fluctuations of constant amplitude between 20 and 500 Hz. The range of frequencies at which sufficient pressure fluctuations were output for the calibration procedure was 80–500 Hz with the white-noise input. Modifying the white-noise signal has therefore increased the range of frequencies to which this technique can be applied.

This signal was then utilized to calculate the response functions of the Scanivalve tappings. Data were acquired simultaneously by pressure transducers at the input (speaker) and output (Scanivalve unit) of the tube. Hence the pressures histories measured at the tapping and the Scanivalve unit were $p(t)$ and $p * r$, respectively,

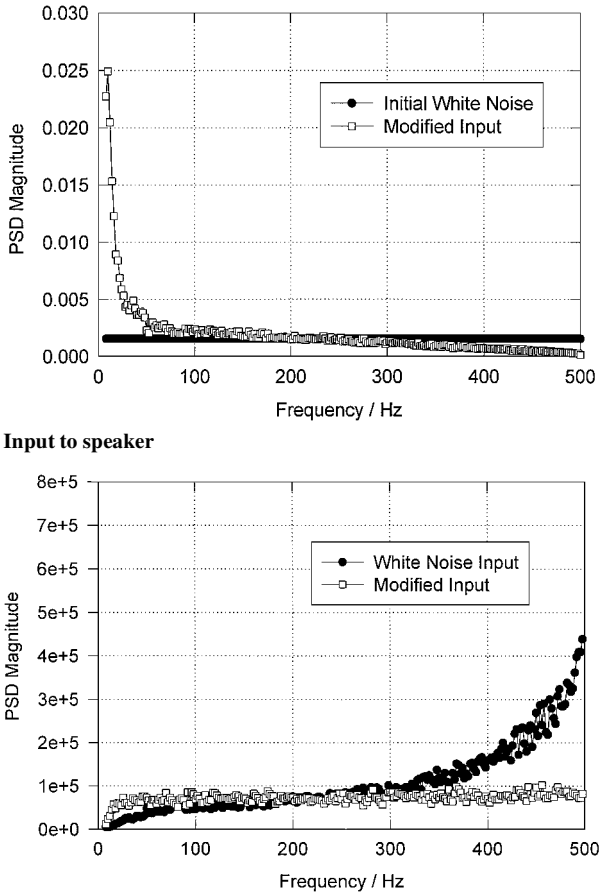

Fig. 5 Calibration inputs and outputs.

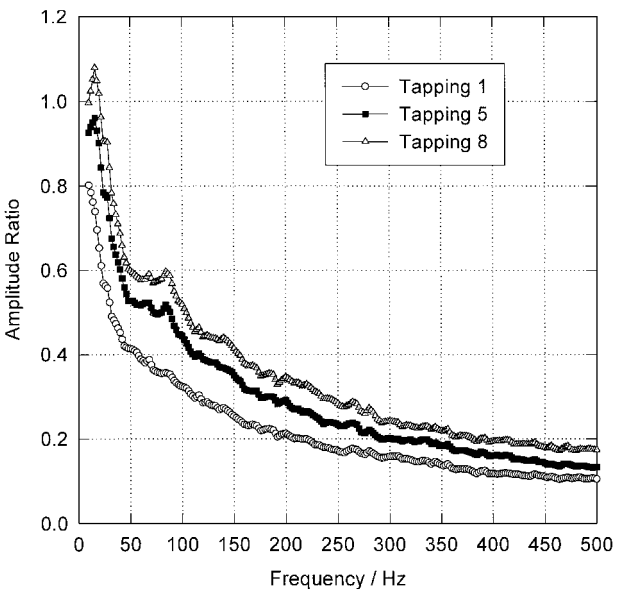

Fig. 6 Example amplitude ratios.

where $p * r$ indicates the convolution of the pressure fluctuation and the response of the tubing. Therefore $r(f)$ could be calculated simply by dividing the complex Fourier transform of $p * r$ by $p(f)$. Each Scanivalve tube that was used was cut to the same length, 2.1 m, to minimize the variation in the response functions. However, variations in the internal dimensions of the tubes necessitated that each tapping was calibrated individually. A comparison of $r(f)$ for a small number of tubes is depicted in Fig. 6. The small peaks apparent

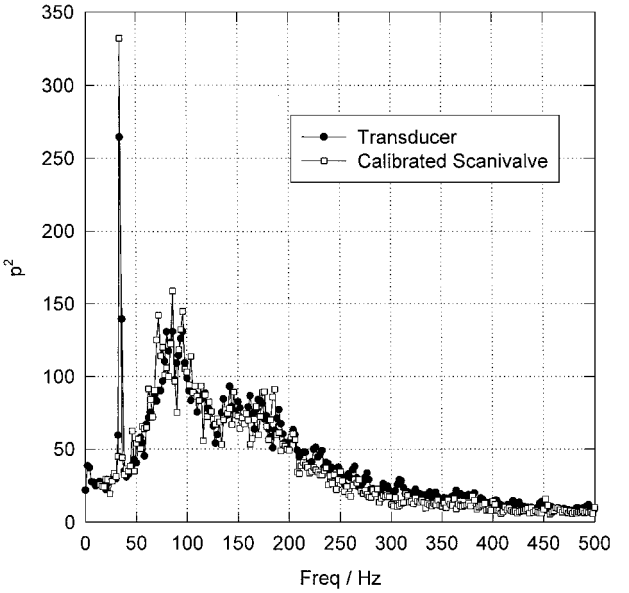

Fig. 7 Transducer–calibrated Scanivalve comparison.

in the amplitude ratios at frequencies in the region of 50–100 Hz are due to standing waves' being set up in the tubes, in a similar manner to those utilized in organ pipes. Variations in the amplitude of the input pressure fluctuations had no impact on the response function of the tubing used during these experiments, although such variations have been noted when the response of shorter tubes was examined.[9]

A comparison between the PSDs experienced during wind-tunnel testing of a calibrated tube and a surface-mounted pressure transducer is shown in Fig. 7. The pressure transducer was mounted in the wing approximately 5 mm from the Scanivalve tapping. This diagram clearly shows that the calibrated Scanivalve tapping, constructed from low-cost materials, is capable of acquiring data at frequencies of up to 500 Hz that previously required unsteady pressure transducers costing approximately £500.

Wind-Tunnel Testing

The semispan models were tested in the 2.13 × 1.52 m low-speed wind tunnel at the University of Bath. Model incidence could be adjusted in the range ±90 deg, although a typical operating range was from −5 to +40 deg. Results are presented for a tunnel speed of 25 m/s, resulting in a Reynolds number of 1.68×10^6/m. Force and moment data were acquired by using the six-component balance installed above the tunnel test section.

Both buffet and buffeting data were assessed to ensure that suitable repeatability was attained. This was achieved by completing 20 identical tunnel runs and acquiring both buffet and buffeting data for 60 s. The spread of the rms of the signals was then considered against sample time. An example of this is shown in Fig. 8. It is clear from this result that the percentage spread in the rms signals reduces at large acquisition times. These tests were repeated for each tunnel entry, typically near peak buffeting, to achieve consistent repeatability and reliability. Sample times of 30 and 25 s were selected for buffeting and buffet data, respectively. Standard deviations of rms values were less than 1.5% for buffeting and 2.0% for buffet data throughout the incidence range. Sampling duration, rate, and analysis parameters were set to maintain a 2-Hz frequency resolution on all PSDs.

Results

The lift and pitching moments generated by the two models are compared in Fig. 9. The negative lift generated for the models at zero incidences is indicative of the negative camber of the models. At incidences of less than 6 deg, the lift curve slope for the 60-deg-swept y wing was less than that for the 40-deg-swept λ wing. This

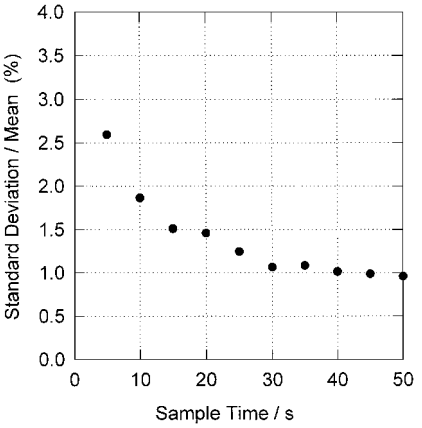

Fig. 8 Evaluation of sample times.

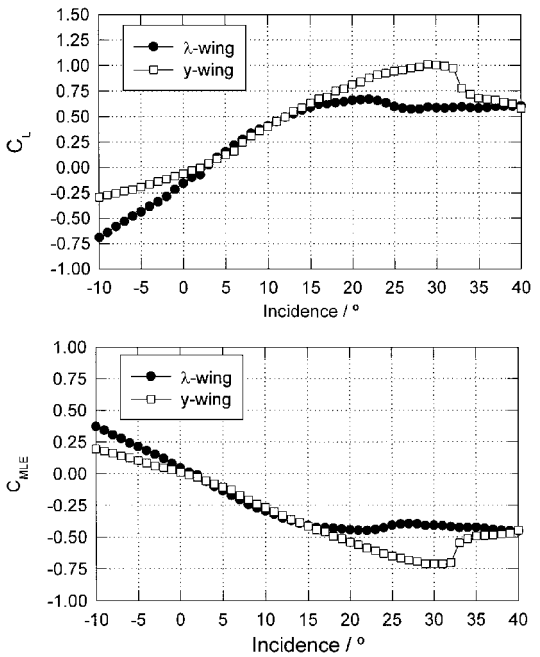

Fig. 9 Lift and pitching moments.

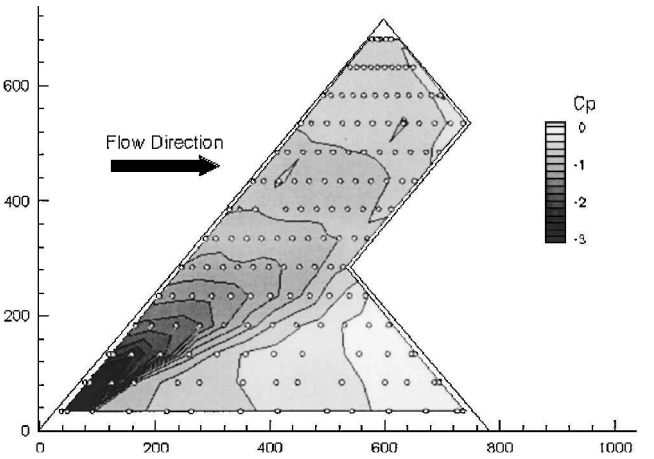

λ wing, α = 14 deg

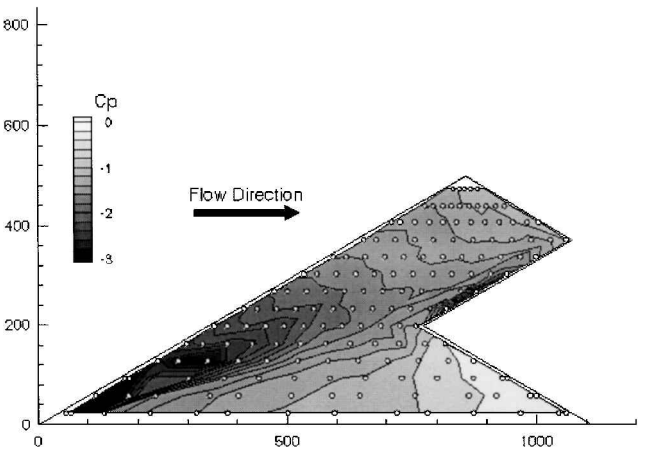

***y* wing, α = 25 deg**

Fig. 10 Mean pressures distributions.

is as would be expected for attached flow over the models, because the aspect ratio of the *y* wing is significantly lower than that of the λ wing (1.93 for the *y* wing compared with 3.98 for the λ wing). As the incidence was increased beyond 6 deg the lift curve slope of the *y* wing increased, as is typical of wings that have energetic vortices over their upper surface.

The effect of the model camber, and its influence on the lower surface flow, can also be noted by examining the lift curves at negative incidences in Fig. 9. If the models had symmetric cross sections, the lift curves at negative incidences would be symmetrical and would pass through the origin. However, as there is negative camber, the vortices formed at negative incidence are weaker than those formed at positive incidences. This is apparent as a reduction in the lift curve slopes at negative incidences. The difference in lift curve slope at positive and negative incidences is more marked for the *y* wing, indicating that the vortex system contributes more to the lift in this case. The almost linear nature of the λ wing's lift curve indicates that the vortex that forms over the wing's upper surface must be very weak.

The *y* wing experienced a sharp decrease in lift in the poststall region. As the incidence was increased beyond 29 deg, there was initially a very slight decrease in lift. However, as the angle of attack was increased from 32 to 33 deg, there was a decrease in the lift generated by the wing, with the lift coefficient dropping from 0.974 to 0.776. If the pitching moments generated by the *y* wing are examined, it can be seen that this dramatic decrease in lift coincided with a sharp increase in the pitching moment about the wing apex, representing an unstable nose-up pitching moment.

An examination of surface flow streaklines indicated that at incidences greater than 20 deg a second vortex, in addition to the leading edge vortex, was present over the upper surface of the *y* wing. This was emanating from the midtrailing edge and grew in strength as the incidence was increased further. As the incidence was increased from 32 to 33 deg, this vortex suddenly broke down and bluff body flow was apparent over the outboard section of the planform. This coincided with the dramatic drop in lift and the nose-up pitching moment experienced by the wing.

Contours of the steady pressure coefficients over the suction surfaces of the two wings are depicted in Fig. 10. These clearly show the characteristic suction peak that is due to leading edge vortices. The magnitude of the suction peak present over the wing with 40 deg of sweep is less than that present over the model with edges swept at 60 deg. There is also a peak along the midtrailing edge of the *y* wing model that is due to the trailing edge vortex at this point. Surface flow visualization indicated that this vortex rotates in the opposite sense to the leading edge vortex. An examination of the diffusion of the suction peaks at a number of spanwise slices[10] enabled estimates to be made of the movement of the vortex burst as the incidence was increased.

Contours of the rms pressure distributions over the two wings are depicted in Fig. 11. There are two distinct differences between the two wings. First, there is an area of very high rms pressures along the midtrailing edge of the *y* wing. This is coincident with the trailing

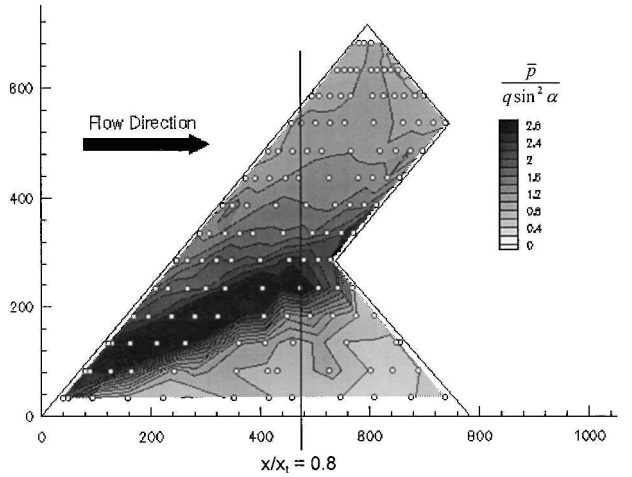

λ wing, α = 14 deg

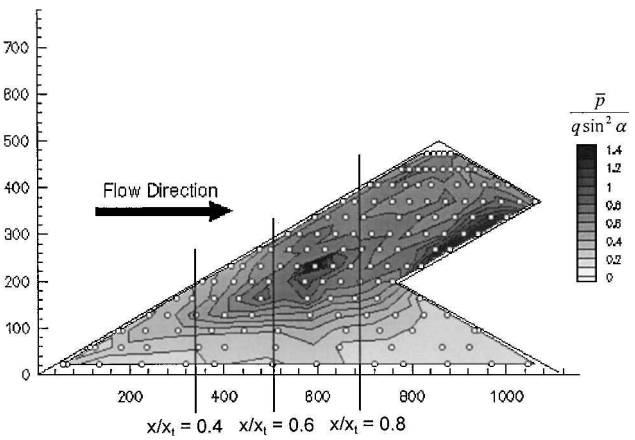

y wing, α = 25 deg

Fig. 11 RMS pressure distributions.

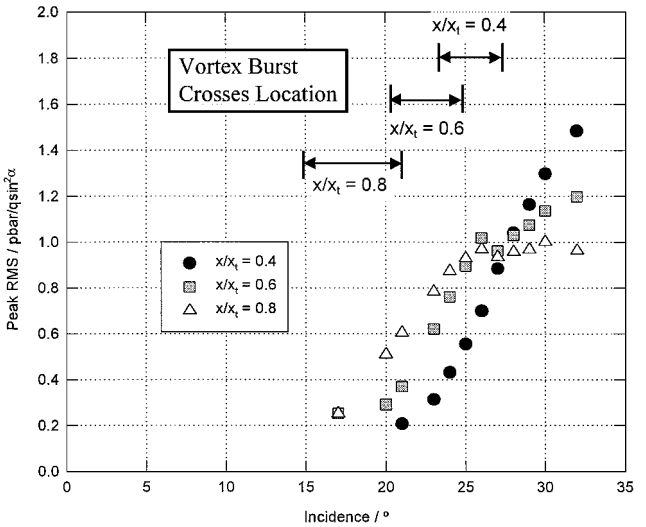

Fig. 12 Variation in rms peaks with incidence and chordwise location.

edge vortex apparent in surface flow visualization and mean pressure measurements, although there is insufficient spatial resolution to detect whether the local peak in the rms pressure fluctuations is under the core or attachment of this vortex. Furthermore, whereas the maximum rms pressure is approximately constant from the apex to the trailing edge for the λ wing, there is a distinct drop in the maximum rms pressure as the leading edge is approached for the model with edges swept at 60 deg. The variation in the magnitude of the rms pressure peaks as the incidence was increased is depicted in Fig. 12 for three chordwise locations. As is clear from this figure, the rise in the rms pressure follows the vortex burst, such that there is little buffet upstream of the burst. This has been noted in many previous investigations of velocity and pressure fluctuations[6,10,11] and thus would have been included in any prediction scheme based on previous data.

Comparisons of the mean and rms pressure distributions for the two models at spanwise slices are depicted in Figs. 13 and 14. Previous work[5] had indicated that the maximum rms pressures were detected just inboard of the core of the leading edge vortex, and this can be seen to be true for the λ wing data depicted in Fig. 13. This result is significant for the development of predictive techniques, as previous work would have placed the location of maximum rms pressure under the core of the vortex. However, for the y-wing data shown in Fig. 14, the location of the maximum rms pressure relative to the leading edge vortex varied as the incidence was changed. At an incidence of 15 deg, the peak rms pressure fluctuations were present outboard of the leading edge vortex suction peak. As the incidence was increased to 20 deg, two peaks were present. The first, and largest, of these was present just outboard of the suction peak, whereas the second was found further outboard. At an incidence of 25 deg, peaks are apparent just outboard and inboard of the vortex core.

The spanwise locations of the secondary separation of the leading edge vortex system are indicated in Fig. 14. These locations were measured from surface flow visualization of the flow. The peaks in the rms pressure distributions that are furthest outboard are therefore coincident with the secondary separations of the leading edge vortex systems. This phenomenon was noted when a pitching delta wing with a leading edge sweep of 60 deg was examined.[12] It is worth noting that at an incidence of 15 deg the only peak present in the spanwise rms pressure distribution is coincident with the secondary separation location. The peak outboard of the suction peak becomes apparent at an incidence of 20 deg. The midtrailing edge vortex becomes apparent at the same incidence.

A small number of sample PSDs in the trailing edge region of the y-wing model are depicted in Fig. 15, together with a PSD from a tapping located away from this region toward the leading edge of the wing. There is a distinct peak at a frequency of approximately 50 Hz in each case. An examination of the PSDs at a variety of freestream speeds confirmed that this peak was not a structural mode, because the frequency scaled with freestream velocity. The presence of this sharp frequency peak upstream of the trailing edge system indicates that pressure fluctuations present in the region of the trailing edge have propagated upstream. This has important repercussions for the development of predictive tools, as the upstream propagation of unsteadiness must be incorporated into any predictions for planforms where there are multiple vortices.

The center frequencies of the buffet experienced over the y-wing model are depicted in Fig. 16. The spectrum at each tapping on the wing was examined and a curve-fitting program was utilized to discern the frequencies of the peaks in the spectra. The frequencies present toward the trailing edge of the model, under the midtrailing edge vortex, form a continuous distribution with those found toward the wing apex. A line of constant reduced-modified reduced-frequency parameter, $n_m = 0.75$, where

$$n_m = f x \sin\alpha / U$$

is superimposed on the graph. Additional peaks are also present at frequencies approximately double those of the low-frequency peaks, although a large amount of scatter is present in this region. The tappings at which these are experienced are located inboard of the core of the vortex. Similar peaks have previously been reported for the λ wing.[5] The frequencies at which the peaks in the spectra are present are approximately 70% higher than those reported by Gursul[6] for 60-deg delta wings at an incidence of 25 deg.

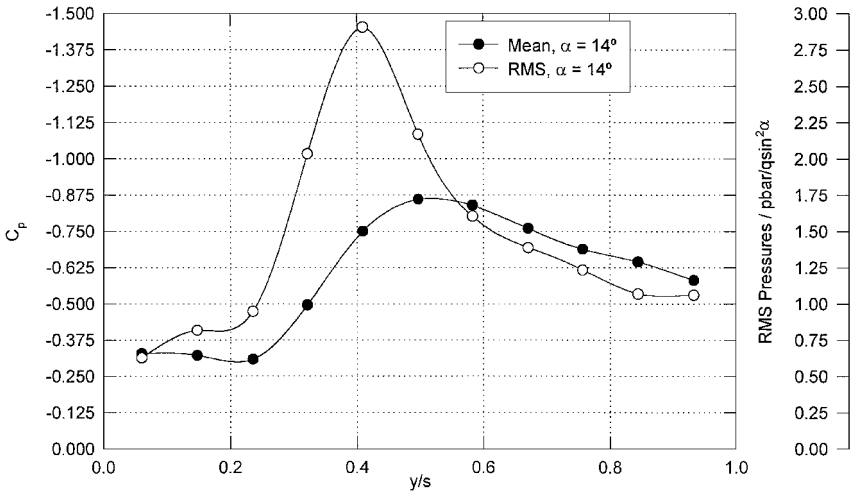

Fig. 13 Spanwise variation of mean and rms pressures; λ wing, $x/x_t = 0.8$.

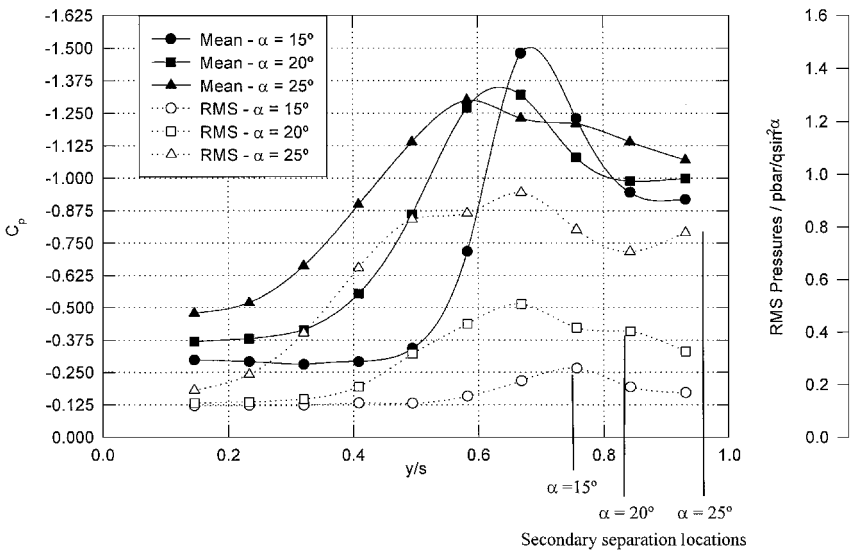

Fig. 14 Spanwise variation of mean and rms pressures; λ wing, $x/x_t = 0.8$.

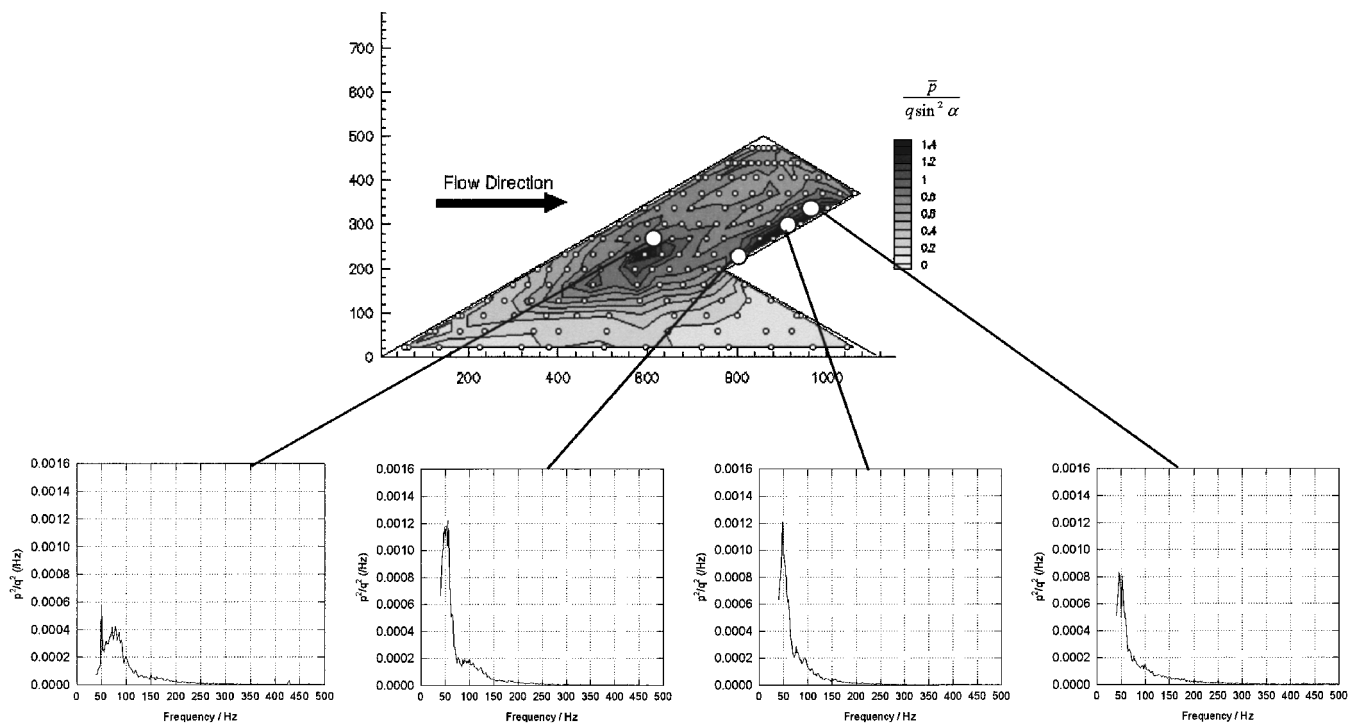

Fig. 15 Sample PSDs over the *y* wing.

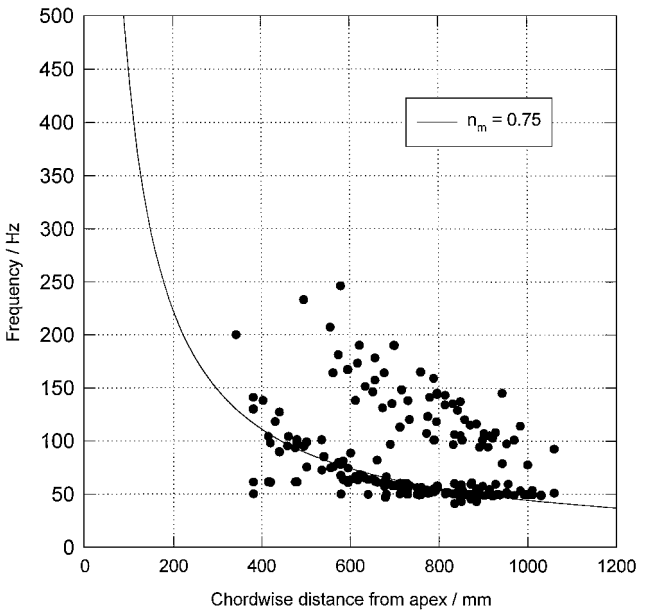

Fig. 16 Center frequencies.

Conclusions

An unsteady pressure measurement technique has allowed unsteady pressures at frequencies of up to 500 Hz to be measured by using a standard Scanivalve installation. The detailed coverage of the wing upper surface has enabled features of the separated flow to be observed in more detail than before at a significantly reduced cost compared with conventional techniques.

Each planform has a leading edge vortex present over its suction surface. In addition, the *y* wing has a vortex present along its trailing edge at incidences higher than 20 deg. This has a dramatic effect on the forces and moments experienced by the wing, leading to a rapid drop in lift coupled with an unstable pitching moment in the poststall region.

The λ-wing model has a single vortex present over its suction surface and the maximum rms pressures are detected inboard of the vortex core. In contrast, the *y*-wing model's maximum rms pressures are experienced outboard of the core of the vortex, with a secondary peak present inboard of the core. A third peak in the spanwise rms pressure distribution has been shown to be coincident with the secondary separation location of the leading edge vortex.

Acknowledgments

This research was funded by the Engineering & Physical Sciences Research Council under Grant GR/J86902 in collaboration with British Aerospace (MA&A), RD1 Ref. WAP04GAAN, R&D Activity 2.3.A.3.

References

[1]Herbst, W. B., "Dynamics of Air Combat," *Journal of Aircraft*, Vol. 20, No. 7, 1983, pp. 594–598.

[2]Mabey, D. G., "Some Aspects of Aircraft Dynamic Loads Due to Flow Separation," *Progress in Aerospace Sciences*, Vol. 26, No. 2, 1989, pp. 115–151.

[3]Hubner, J. P., and Komerath, N. M., "Spectral Mapping of Quasi-Periodic Structures in a Vortex Flow," *Journal of Aircraft*, Vol. 32, No. 3, 1995, pp. 493–500.

[4]Rediniotis, O. K., Stapountzis, H., and Telionis, D. P., "Periodic Vortex Shedding over Delta Wings," *AIAA Journal*, Vol. 31, No. 9, 1993, pp. 1555–1562.

[5]Woods, M. I., and Wood, N. J., "Unsteady Aerodynamic Effects on a Generic Series of Novel Planforms," *Royal Aeronautical Society Conference on Unsteady Aerodynamics*, London, U.K., July 1996, pp. 14.1–14.10.

[6]Gursul, I., "Unsteady Flow Phenomena over Delta Wings at High Angles of Attack," *AIAA Journal*, Vol. 32, No. 2, 1994, pp. 225–231.

[7]Pilkington, D. J, and Wood, N. J., "Unsteady Aerodynamic Effects of Trailing Edge Controls on Delta Wings," *The Aeronautical Journal*, Vol. 99, No. 983, 1995, pp. 99–108.

[8]Vaughan, J. P., and Wood, N. J., "Pressure Measurements on a Half Delta Wing Oscillating in Pitch," *The Aeronautical Journal*, Vol. 99, No. 990, 1995, pp. 432–438.

[9]Lynn, R. J., "Dynamic Calibration of Tube-Transducer Systems for Unsteady Pressure Measurement," Defence Evaluation and Research Agency Bedford, DERA/AS/HWA/TR980022, Bedford, U.K., Jan. 1998.

[10]Greenwell, D. I., and Wood, N. J., "Determination of Vortex Burst Location on Delta Wings from Surface Pressure Measurements," *AIAA Journal*, Vol. 30, No. 11, 1992, pp. 2736–2739.

[11]Jaworski, A. J., "A Study of Pressure Fluctuations Caused by Vortex Breakdown," Ph.D. Dissertation, Dept. of Aeronautics, Imperial College of Science, Technology, and Medicine, London, U.K., 1996.

[12]Jupp, M. L., Coton, F. N., Green, R. B., Galbraith, R. A. M., "An Analysis of a Pitching Delta Wing Using High Resolution Pressure Measurements," AIAA Paper 98-2743, June 1998.